# Influence of Dielectric Anisotropy on the Absorption Properties of Localized Surface Plasmon Resonances Embedded in Si Nanowires

*Li-Wei Chou,*[†] *Rachel D. Near,*[‡] *Dmitriy S. Boyuk,*[†] *and Michael A. Filler*[*,†]

[†] School of Chemical & Biomolecular Engineering, Georgia Institute of Technology, Atlanta 30332, Georgia, United States

[‡] School of Chemistry and Biochemistry, Georgia Institute of Technology, Atlanta 30332, Georgia, United States

[*] E-mail: michael.filler@chbe.gatech.edu

## 1. Simulation methods

Simulations of nanowire spectral response were accomplished within the discrete dipole approximation (DDA) using the DDSCAT 6.1 code.[1-4] Isolated Si resonators as well as those embedded in nanowires were approximated as a collection of point dipoles periodically arranged into cylinders (Supporting Information, Figure S1). The response of each point dipole under the influence of an incident electric field (E-field) and neighboring dipoles was computed self-consistently by coupling complex-conjugate gradient and fast-Fourier transform methods.[2] Spectral extinction ($Q_{ext}$), absorption ($Q_{abs}$), and scattering ($Q_{scat}$) efficiencies (i.e., the far-field properties) as well as E-field enhancement and polarization vectors (i.e., the near-field properties) were then calculated from these responses. The polarization dependence of the spectral response was determined for applied E-field polarizations as shown in Figure S1. Alignment of the applied E-field along the y-axis and x-axis provides access to the longitudinal and transverse excitations, respectively.

Dipoles located in undoped and doped segments were assigned appropriate optical constants (i.e., *n* and *k* values). Figures S2(a) and S2(b) show plots of *n* and *k*, respectively, from 2 to 20 μm (5000 to 500 $cm^{-1}$) taken from Palik and used for all undoped segments (i.e., CdS, CdSe, GaP, GaAs, Si, and Ge).[5] The optical constants for doped Si segments were determined via the Drude model, which has been widely utilized for this purpose,[5-7] and can be expressed as:

$$\varepsilon(\omega) = (n + ik)^2 = \varepsilon_\infty - \frac{\omega_p^2}{\omega \cdot (\omega + i\gamma)} \tag{1-1}$$

where $\varepsilon_\infty$ (~11.7) is the dielectric constant of pure Si,[8] $\omega$ is the incident light frequency, $\omega_p$ is bulk plasma frequency, and $\gamma$ is scattering time. As tabulated in Table S4, values for the bulk plasma frequency and scattering time were calculated as a function of carrier density, $N_e$, via:

$$\omega_p^2 = \frac{N_e \cdot q^2}{\varepsilon_\infty \cdot m_e} \tag{1-2}$$

$$\gamma = \frac{q}{\mu_e \cdot m_e} \tag{1-3}$$

where $q$ is elementary charge, $m_e$ is effective mass, and $\mu_e$ is the electron mobility. $m_e$ and $\mu_e$ are well known as a function of $N_e$ for Si and also included in Table S4.[5,9] Figures S2(c) and S2(d) show the *n* and *k* values, respectively, calculated for doped Si. The similarity of theses values with those from Palik at carrier densities below $10^{20}$ $cm^{-3}$ supports the application of the Drude model for carrier densities above $10^{20}$ $cm^{-3}$.

An error tolerance (TOL) less than $10^{-3}$ and a periodic dipole grid spacing of 10 nm were selected to optimize simulation accuracy and computational cost. All nanowires with embedded doped segments contained a total of 8905 dipoles – 13 in the radial direction and 65 in the axial direction – to best match the experimentally synthesized nanowire morphology (i.e., $l_{\text{total}}$ = 650 nm and $d$ = 130 nm). To ensure that this grid spacing was appropriate for the resonators studied here, simulations with stricter TOL values and smaller grid spacings were also completed. Figure S3(a) shows the simulated extinction spectra at multiple TOL values for the longitudinal excitation of an embedded doped segment with an aspect ratio of 0.4 and carrier density of $2.3 \times 10^{20}$ cm$^{-3}$. A residual analysis is displayed in Figure S3(b). The residual is defined as

$$\text{Residual} = Q_{ext}(\omega, \text{TOL}) - Q_{ext}(\omega, \text{TOL} = 10^{-6}) \tag{1-4}$$

where $Q_{ext}(\omega, \text{TOL})$ is the simulated extinction efficiency as a function of frequency, $\omega$, at a particular TOL value. A maximum residual of $4 \times 10^{-5}$ is obtained for a TOL of $10^{-3}$, which supports the use of this TOL to describe our Si-based resonators. Figure S4 shows the simulated extinction spectra and E-field enhancement maps at dipole spacings of 3.3, 5.0 and 10.0 nm for the longitudinal excitation of embedded and isolated Si resonators with two different aspect ratios. Figure S4 reveals minimal differences in simulated extinction spectra and E-field enhancement for all grid spacings and both resonator geometries, which confirms that a grid spacing of 10 nm is appropriate here.

## 2. Estimation of experimental absorption cross-section

The maximum absorption cross-section for each embedded resonator was estimated from *in-situ* infrared spectral response measurements by combining the slab model shown in Figure S12 with the Beer-Lambert Law:[10]

$$2.303 \cdot Abs(\omega_{\max}) = Abs^{*}(\omega_{\max}) = \sigma(\omega_{\max})_{\exp} \cdot OPL \cdot N \tag{2-1}$$

where $Abs(\omega_{\max})$ is the maximum experimental absorbance in base 10, $Abs^{*}(\omega_{\max})$ is the maximum experimental absorbance in base $e$, $\sigma(\omega_{\max})_{\exp}$ is the maximum experimental absorption cross-section, $OPL$ is the optical path length, $N$ is the density of doped segments. $N$ can be obtained from:

$$N = \frac{S}{l_{total}} \tag{2-2}$$

where $S$ is the nanowire areal density when projected onto the plane perpendicular to the infrared beam, $l_{total}$ is the total nanowire length (fixed at 0.65 μm here). The optical path length ($OPL$) is

defined as the distance traveled by the incident photon through the nanowire as illustrated in Figure S12. For an angle of incidence of 58°, which is where the longitudinal excitation is maximized in our experiments, the *OPL* can be extracted from:

$$OPL = \frac{l_{total}}{\cos(58°)} \tag{2-3}$$

where $\theta$ is the angle of incidence. By substituting values of $N$ and $OPL$ from equations (2-2) and (2-3), respectively, into equation (2-1), $\sigma(\omega_{\max})_{\exp}$ of any nanowire can be obtained. Values for a range of embedded resonator aspect ratios are extracted and tabulated in Table S3.

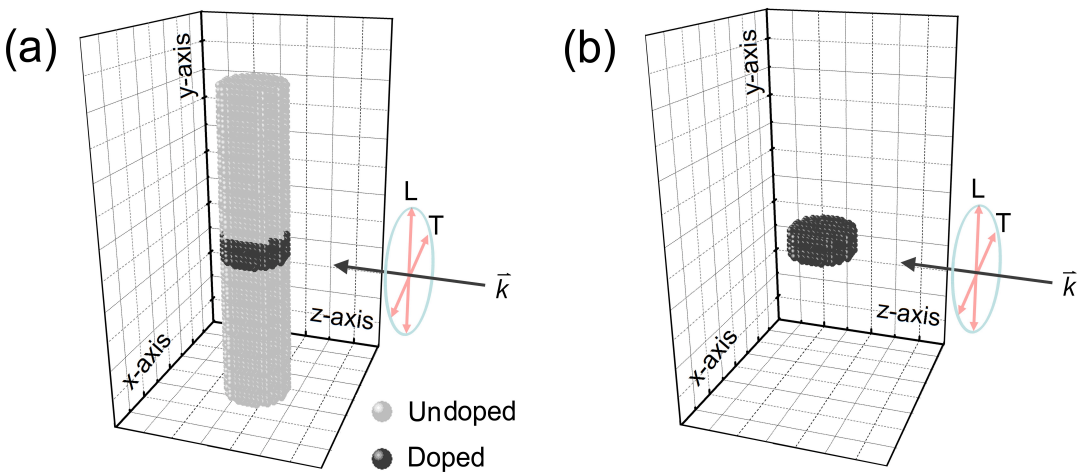


**Figure S1.** Simulation models of (a) embedded and (b) isolated Si resonators (i.e., doped segments) with an aspect ratio of 0.4. Dark and light gray colored dipoles represent doped and undoped segments, respectively. An applied E-field (*k,* a black arrow) propagating along the z-axis can be designed with a polarization (a red arrow) along either the x- or y-direction to enable transverse (T) or longitudinal (L) excitation, respectively.

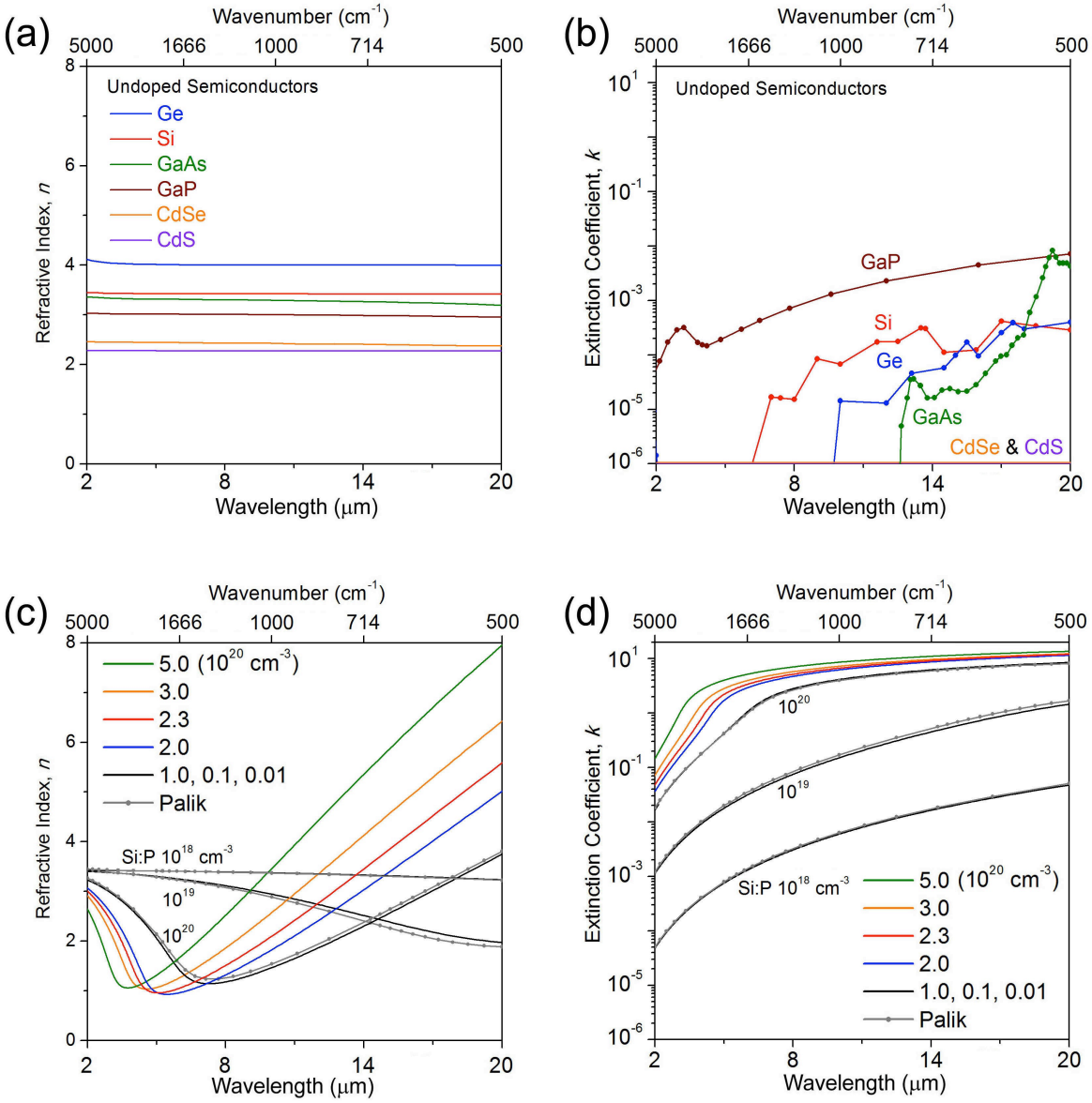


**Figure S2.** Optical constants utilized for DDA simulations. (a) Refractive index, $n$, and (b) extinction coefficient, $k$, as a function of wavelength for intrinsic Ge, Si, GaAs, GaP, CdSe and CdS.[5] $k$ values below $10^{-6}$ were set to zero in the simulations. (c) $n$ and (d) $k$ values for doped Si ($1 \times 10^{18} - 5 \times 10^{20}$ cm$^{-3}$) as determined from the literature values tabulated in Table S4 and equations (1-1) to (1-3). Values of doped Si from Palik are also plotted for comparison.[5]

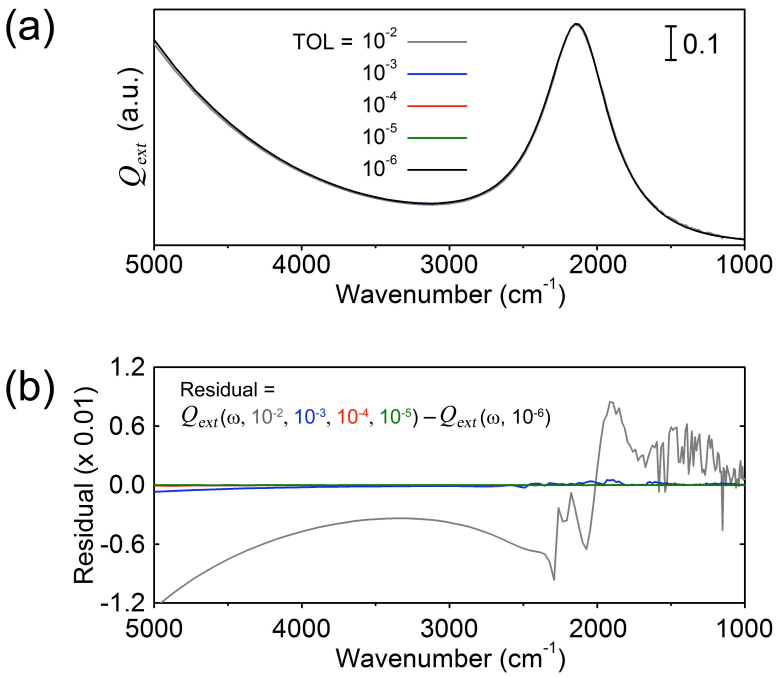


**Figure S3.** Simulation error tolerance (TOL) analysis. (a) Simulated extinction efficiencies ($Q_{ext}$) of the longitudinal excitation for an embedded Si resonator at multiple error tolerances (TOL = $10^{-2}$, $10^{-3}$, $10^{-4}$, $10^{-5}$ and $10^{-6}$). (b) Residual analysis as a function of frequency and TOL value indicates that a TOL of $10^{-3}$ provides good convergence. Doped segment aspect ratio, carrier density, and dipole grid spacing are 0.4, $2.3 \times 10^{20}$ $cm^{-3}$, and 10 nm, respectively.

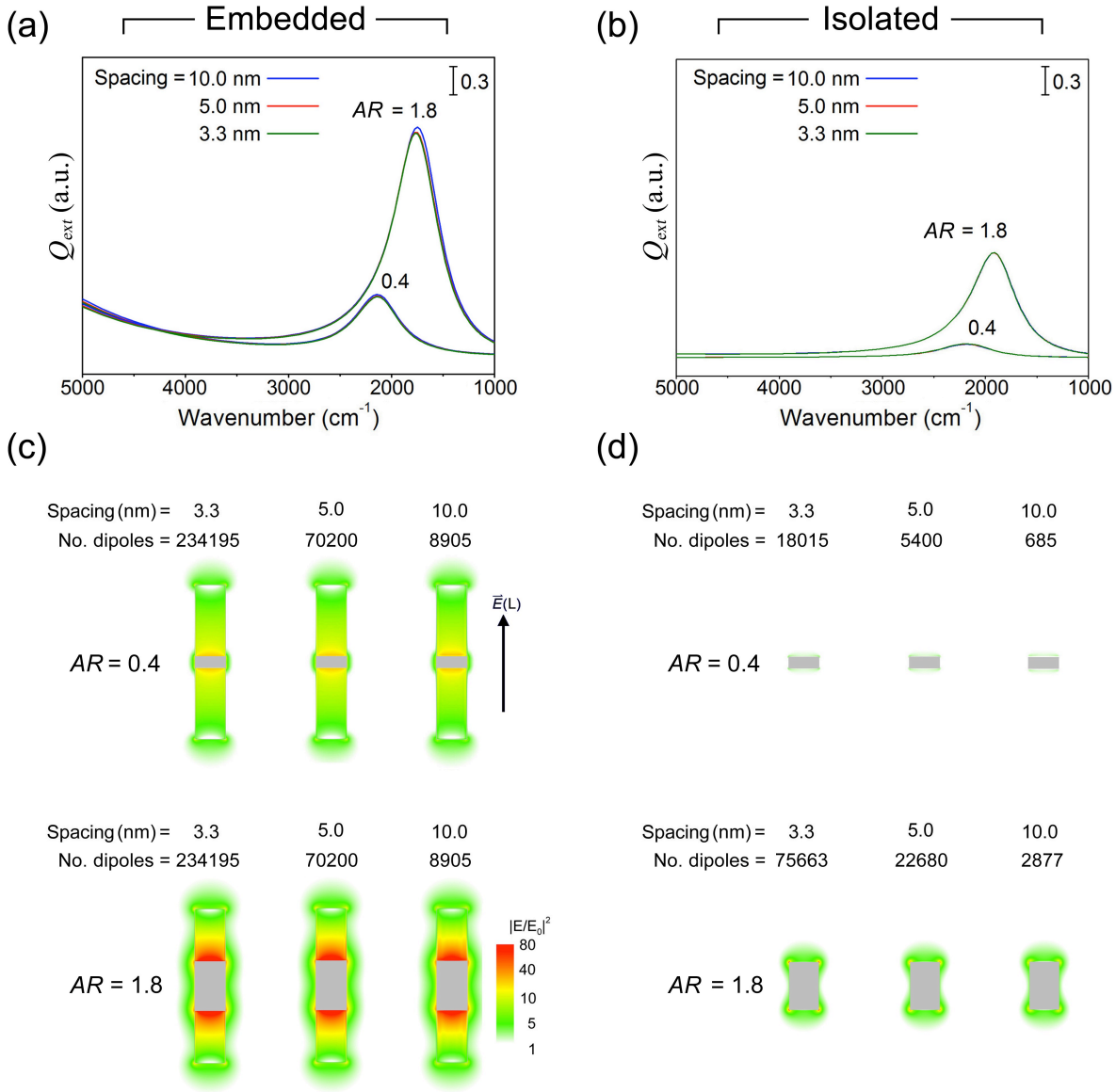


**Figure S4.** Simulation dipole grid spacing analysis. (a) - (b) Calculated extinction efficiencies ($Q_{ext}$) and corresponding (c) - (d) E-field enhancement maps for the longitudinal (L) excitation of embedded and isolated Si resonators ($AR$ = 0.4 and 1.8) with dipole grid spacings of 3.3, 5.0 and 10.0 nm. Doped segments are colored grey. E-field enhancement is denoted by a red-to-green gradient. The similarity of extinction efficiency and E-field enhancements for all dipole grid spacings validates the use of 10.0 nm in the present work. Doped segment carrier density is $2.3 \times 10^{20}$ cm$^{-3}$ and error tolerance (TOL) is fixed at $10^{-3}$. A black arrow represents an applied field, E(L).

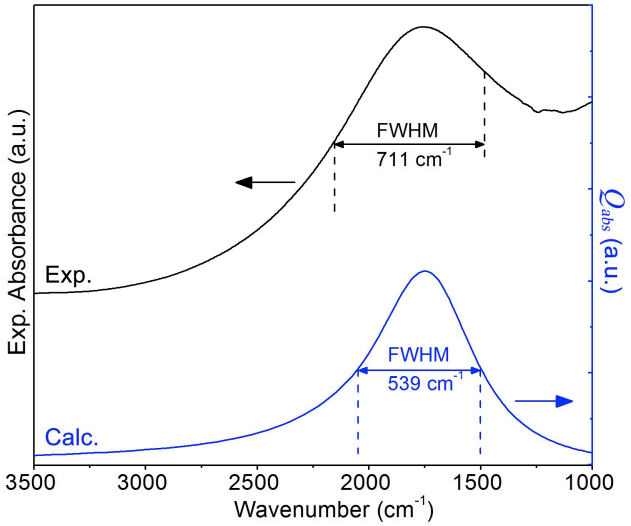


**Figure S5.** Comparison of the experimental and simulated peak broadening for the longitudinal excitation of embedded Si resonators with an aspect ratio of 1.8. Experimental *in-situ* infrared absorption measurement (black curve) for a Si nanowire array with an areal density of 0.6 $\mu m^{-2}$, doped segment $C$ (= $P_P/P_{Si}$) value of 0.05, and measured at an angle of incidence of 58°. Simulated absorption efficiency ($Q_{abs}$, blue curve) with a doped segment carrier density of $2.3 \times 10^{20}$ $cm^{-3}$.

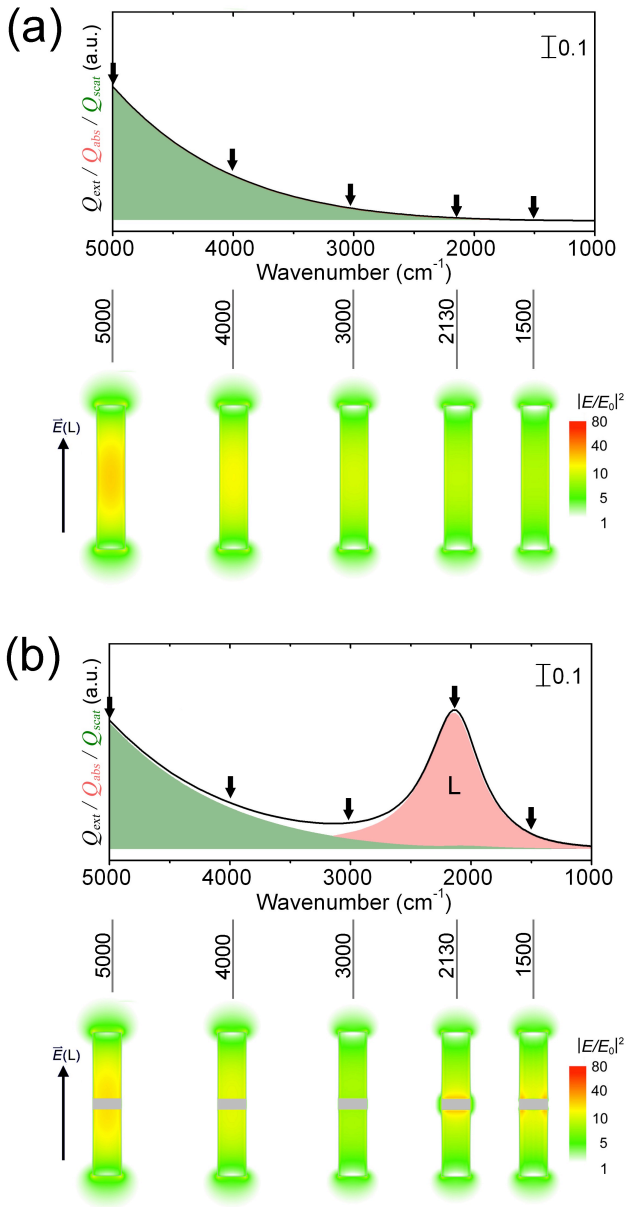


**Figure S6.** Simulated extinction ($Q_{ext}$, solid black line), absorption ($Q_{abs}$, red shading), and scattering ($Q_{scat}$, green shading) efficiencies and frequency-dependent E-field enhancement maps of the longitudinal excitation for Si nanowires that are (a) undoped and (b) contain an embedded resonator with an aspect ratio of 0.4 and carrier density of $2.3 \times 10^{20}$ cm$^{-3}$. E-field enhancement is denoted by a red-to-green gradient. Absorption results from the embedded resonator, while scattering stems from the overall nanowire length. A black arrow represents an applied field, E(L).

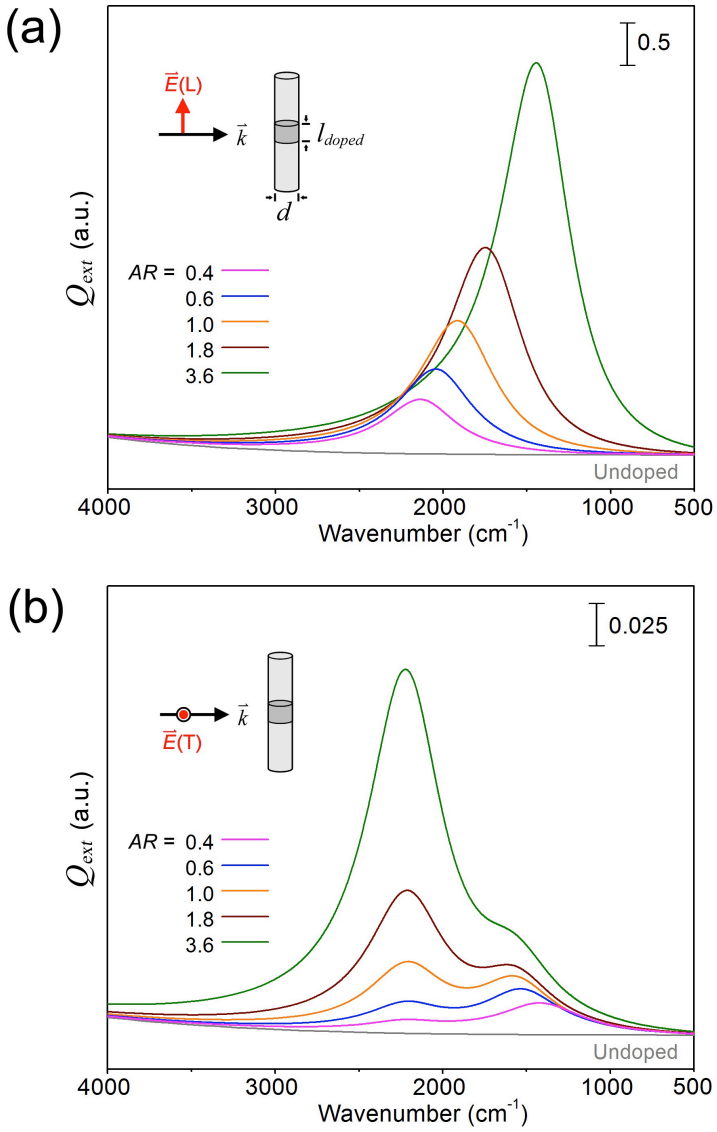


**Figure S7.** Simulated extinction efficiencies ($Q_{ext}$) of the (a) longitudinal and (b) transverse excitation of embedded Si resonators with a range of aspect ratios ($AR = l_{doped}/d$ = 0.4, 0.6, 1.0, 1.8 and 3.6) and a fixed carrier density of $2.3 \times 10^{20}$ cm$^{-3}$. An undoped nanowire is included for comparison in both cases. Notably, the maximum extinction efficiency for the longitudinal excitation at each aspect ratio is more than 20 times larger than the transverse excitation. Insets: schematic illustration of the applied E-field for both polarizations.

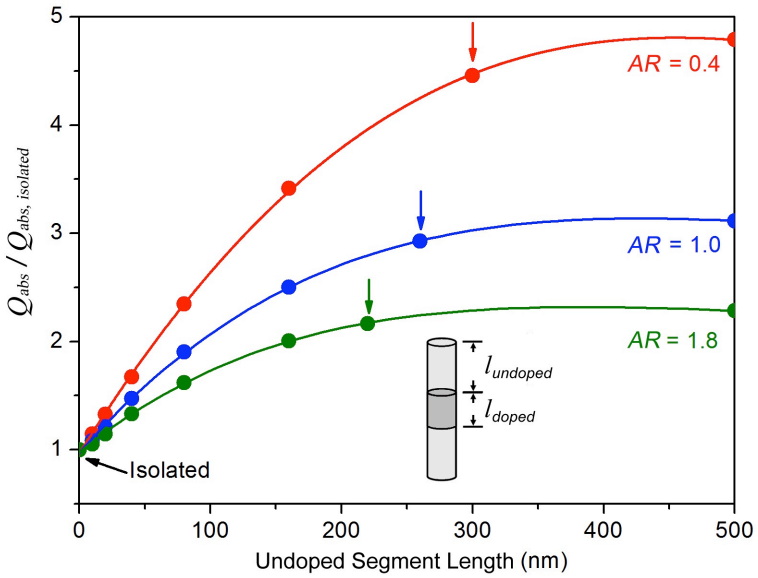


**Figure S8.** Simulated absorption efficiency of the longitudinal excitation for Si resonators with aspect ratios of 0.4, 1.0, and 1.8 cladded by undoped Si segments of different lengths ($l_{undoped}$ = 0 to 500 nm) relative to that for isolated resonators (i.e., $l_{undoped}$ = 0) with the same aspect ratio. Doped segment carrier density is fixed at 2.3 × $10^{20}$ $cm^{-3}$. The smallest aspect ratio yields the largest increase in absorption ($AR$ = 0.4). Nanowire diameter is fixed at $d$ = 130 nm and doped segment lengths are $l_{doped}$ = 50 ($AR$ = 0.4), 130 ($AR$ = 1.0) and 230 ($AR$ = 1.8) nm.

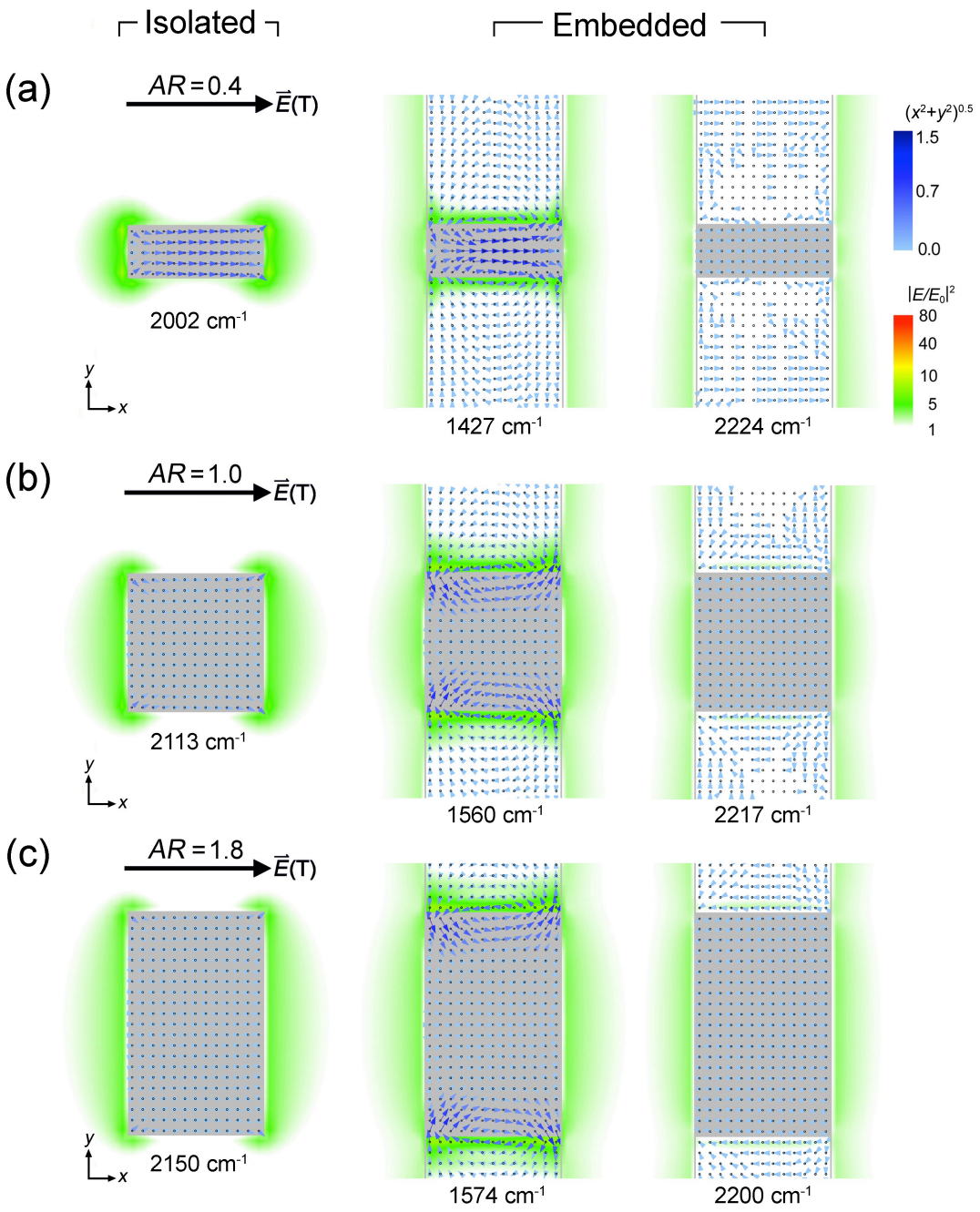


**Figure S9.** Combined polarization vector and E-field enhancement maps calculated at the absorption efficiency maxima for the transverse excitations of embedded and isolated Si resonators with aspect ratios of 0.4, 1.0 and 1.8. Doped segment carrier density is fixed at 2.3 × $10^{20}$ $cm^{-3}$. Small arrows represent the vector direction and magnitude of each dipole under the influence of the applied E-field (denoted by a black arrow). Vector magnitude and field enhancement are denoted by blue and red-to-green gradients, respectively.

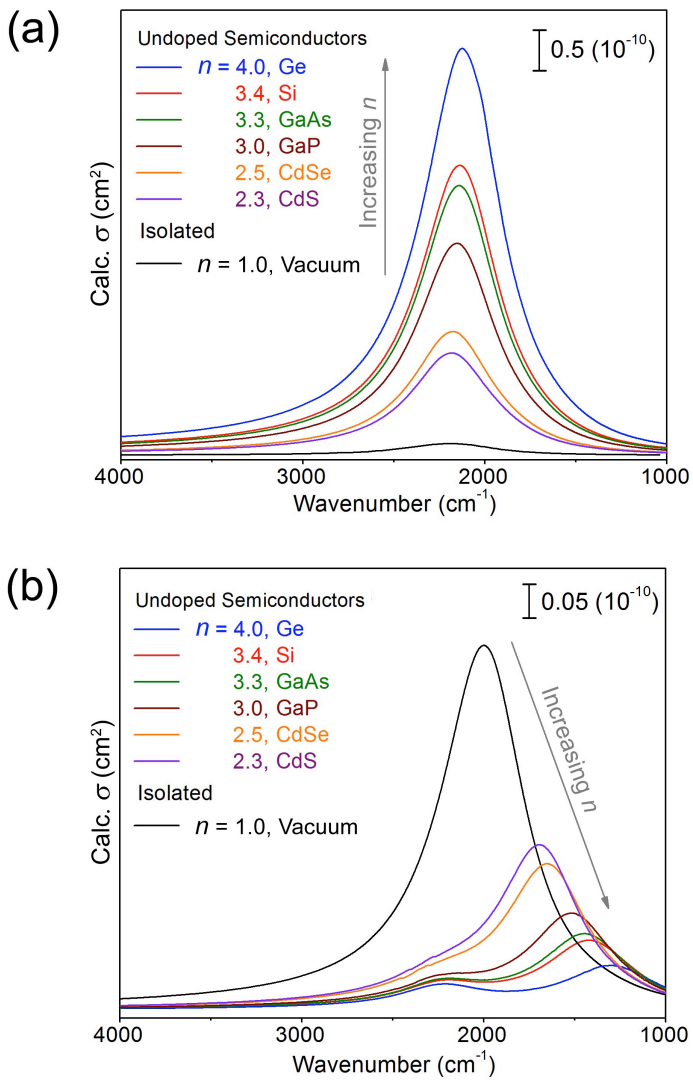


**Figure S10.** Simulated absorption cross-section of (a) longitudinal and (b) transverse excitations of Si resonators with an aspect ratio of 0.4 embedded in various undoped semiconductor. Doped segment carrier density is fixed at $2.3 \times 10^{20}$ $cm^{-3}$. The absorption enhancement and depression of the longitudinal and transverse excitations scales with refractive index, respectively, as indicated by grey arrows.

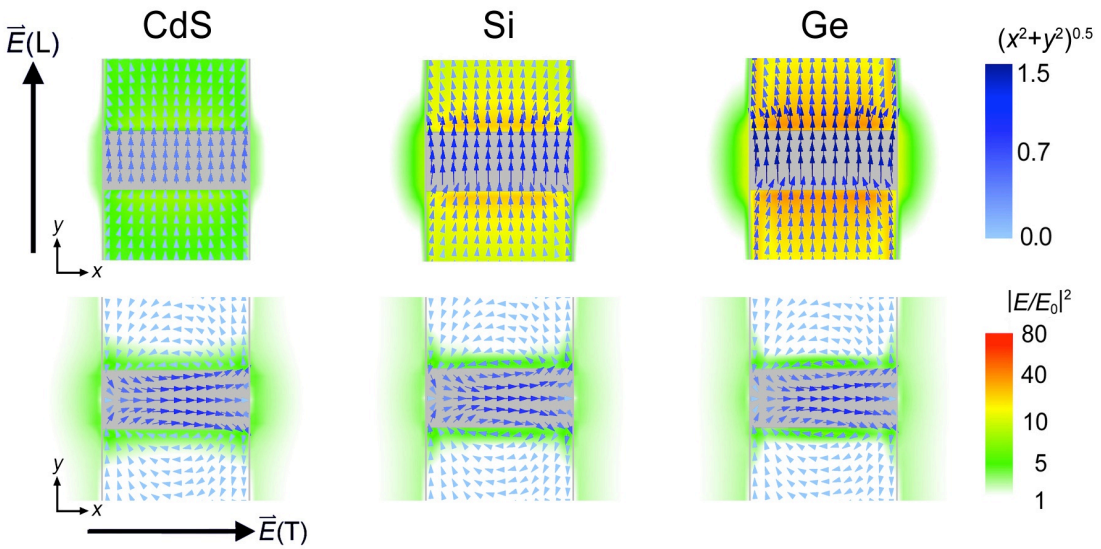


**Figure S11.** Combined polarization vector and E-field enhancement maps simulated at the longitudinal and transverse excitation absorption efficiency maxima for Si resonators with an aspect ratio of 0.4 embedded in undoped CdS, Si, and Ge segments. Doped Si segment carrier density is fixed at $2.3 \times 10^{20}$ $cm^{-3}$. Small arrows represent the vector direction and magnitude of each dipole under the influence of the applied E-field (denoted by a black arrow). Vector magnitude and E-field enhancement are denoted by blue and red-to-green gradients, respectively.

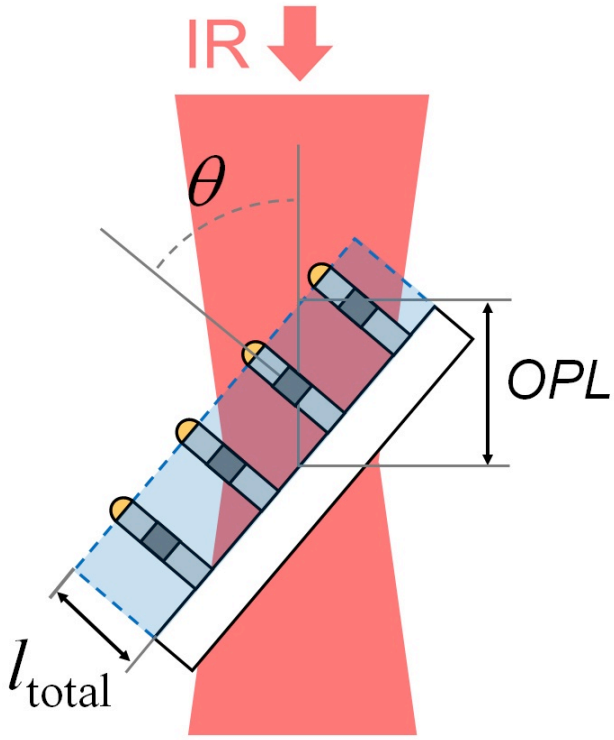


**Figure S12.** Schematic illustration of measurement geometry and identification of the optical path length (*OPL*). Nanowires of overall length, $l_{total}$, are situated on a Si(111) substrate. Note that the substrate is only present during experiment.

| | Embedded | Peak Characteristics | | Derived Values | |
|---|---|---|---|---|---|
| | $AR$ | $\omega_{max}$ | FWHM ($cm^{-1}$) | $\gamma$ (meV) | $QF$ |
| Exp. | 0.4 | 2085 | 659 | 83 | 3.1 |
| | 0.6 | 2000 | 703 | 90 | 2.8 |
| | 1.0 | 1895 | 696 | 91 | 2.6 |
| | 1.8 | 1791 | 711 | 92 | 2.4 |
| | 3.6 | 1466 | 715 | 80 | 2.3 |
| Calc. | 0.4 | 2138 | 540 | 66 | 4.1 |
| | 0.6 | 2050 | 545 | 66 | 3.9 |
| | 1.0 | 1920 | 546 | 67 | 3.7 |
| | 1.8 | 1749 | 539 | 66 | 3.4 |
| | 3.6 | 1447 | 510 | 62 | 3.0 |

**Table S1.** Comparison of experimental and simulated longitudinal excitation peak characteristics for embedded Si resonators as a function of aspect ratio ($AR = l_{doped}/d$): $\omega_{max}$, maximum absorption frequency; FWHM, full-width at half-maximum; $\gamma$, collision frequency; $QF$, quality factor.

| | Embedded | | | |
|---|---|---|---|---|
| *AR* | Longitudinal Mode | | Transverse Mode | |
| | $\omega_{max}$ (cm$^{-1}$) | $Q_{abs,\,max}$ | $\omega_{max}$ (cm$^{-1}$) | $Q_{abs,\,max}$ |
| 1.8 | 1749 | 2.43 | 2220, 1574 | 0.081, 0.028 |
| 1.0 | 1920 | 1.58 | 2217, 1560 | 0.038, 0.028 |
| 0.4 | 2138 | 0.64 | 2224, 1427 | 0.007, 0.019 |
| | Isolated | | | |
| 1.8 | 1921 | 1.13 | 2150 | 0.375 |
| 1.0 | 2047 | 0.54 | 2113 | 0.407 |
| 0.4 | 2190 | 0.14 | 2002 | 0.546 |

**Table S2.** Simulated longitudinal and transverse excitation peak characteristics for embedded and isolated Si resonators as a function of aspect ratio ($AR = l_{doped}/d$): $\omega_{max}$, maximum absorption frequency; $Q_{abs,max}$, maximum absorption efficiency.

| | Nanowire Array Characteristics | | | | Absorption Properties | |
|---|---|---|---|---|---|---|
| *AR* | *S* ($\mu m^{-2}$) | *F* | *N* ($\mu m^{-3}$) | *OPL* ($\mu m$) | Abs ($\omega_{max}$) | $\sigma(\omega_{max})_{exp}$ $10^{-10}$ ($cm^2$) |
| 0.4 | 1.1 | 0.01 | 1.7 | 1.2 | 0.0026 | 0.3 |
| 0.6 | 1.1 | 0.01 | 1.7 | 1.2 | 0.0044 | 0.5 |
| 1.0 | 1.1 | 0.01 | 1.7 | 1.2 | 0.0096 | 1.1 |
| 1.8 | 1.1 | 0.01 | 1.7 | 1.2 | 0.0170 | 1.9 |
| 3.6 | 1.1 | 0.01 | 1.7 | 1.2 | 0.0400 | 4.5 |

**Table S3.** Comparison of experimental and simulated absorption cross-sections for embedded Si resonators as a function of doped segment aspect ratio ($AR = l_{doped}/d$) as extracted from and our previous work[11]. *S*, projected nanowire areal density; *F*, areal fill factor; *N*, volumetric nanowire density; *OPL*, optical path length; Abs($\omega_{max}$), maximum absorption frequency; $\sigma(\omega_{max})_{exp}$, maximum experimental absorption cross-section.

| Carrier Density $N_e$ ($10^{20}$ cm$^{-3}$) | Effective Mass $m_e$ | Electron Mobility $\mu_e$ (cm$^2$/V-sec) | Bulk Plasma $\omega_p$ ($10^{14}$ /sec) | Scattering Time $\gamma$ ($10^{-14}$ s) |
|---|---|---|---|---|
| 0.01 | 0.27 | 277 | 0.17 | 4.26 |
| 0.10 | 0.27 | 115 | 0.55 | 1.77 |
| 1.00 | 0.27 | 73 | 1.70 | 1.17 |
| 2.00 | 0.31 | 57 | 2.28 | 1.10 |
| 2.30 | 0.32 | 56 | 2.40 | 1.06 |
| 3.00 | 0.33 | 48 | 2.71 | 0.93 |
| 5.00 | 0.37 | 33 | 3.30 | 0.69 |

**Table S4.** Literature values of doped Si effective mass,[5] $m_e$, and electron mobility,[9] $\mu_e$, as a function of carrier density, $N_e$. Bulk plasma frequency, $\omega_p$, and scattering time, $\gamma$, are determined via the Drude model and converted to the frequency-dependent optical constants plotted in Figure S2.

## References


(1) Goodman, J. J.; Flatau, P. J.; Draine, B. T. Application of Fast-Fourier-transform Techniques to the Discrete-dipole Approximation. *Optics Letters* **1991**, *16*, 1198-1200.

(2) Draine, B. T.; Flatau , P. J. Discrete-dipole approximation for scattering calculations. *J. Opt. Soc. Am. A* **1994**, *11*, 1491-1499.

(3) Shuford, K. L.; Ratner, M. A.; Schatz, G. C. Multipolar Excitation in Triangular Nanoprisms. J. Chem. Phys. 2005, 123, 114713(1-9).

(4) Draine, B. T.; Flatau, P. J. User Guide for the Discrete Dipole Approximation Code DDSCAT 6.1. [Online Early Access]. Published Online: 2004. http://arxiv.org/abs/astro-ph/0409262.

(5) Palik, E. *Handbook of Optical Constants of Solids*; Academic Press, 1998.

(6) Hesketh, P. J.; Zemel, J. N.; Gebhart, B. Polarized spectral emittance from periodic micromachined surfaces. II. Doped silicon: Angular variation. Phys. Rev. B 1988, 37, 10803-10813.

(7) Basu, S.; Lee, B. J.; Zhang, Z. M. Infrared Radiative Properties of Heavily Doped Silicon at Room Temperature. *J. Heat Transf.* **2009**, *132*, 023301(1-8).

(8) Arai, T. Plasma oscillations in heavily doped n-type silicon. *Proc. Phys. Soc.* **1964**, *84*, 25.

(9) Masetti, G.; Severi, M.; Solmi, S. Modeling of carrier mobility against carrier concentration in arsenic-, phosphorus-, and boron-doped silicon. *Electron Devices, IEEE Transactions on,* **1983**, *30*, 764-769.

(10) Atkins, P.; Paula, J. *Atkins' Physical Chemistry*; 7 ed.; Oxford University press, 2002.

(11) Chou, L.-W.; Filler, M. A. Engineering Multimodal Localized Surface Plasmon Resonances in Silicon Nanowires. *Angew. Chem. Int. Edit.* **2013**, *125*, 8237-8241.